Crustal surface-wave velocity structure of the east Albany-Fraser Orogen, Western Australia, from ambient noise recordings

C. Sippl[1,2], B.L.N. Kennett[1], H. Tkalčić[1], K. Gessner[3], C.V. Spaggiari[3]

[1]*Research School of Earth Sciences, Australian National University, Canberra, Australia*

[2]*Section Lithosphere Dynamics, German Research Centre for Geosciences (GFZ), Potsdam, Germany*

[3]*Geological Survey of Western Australia, Perth, Australia*

SUMMARY

Group and phase velocity maps in the period range 2-20 s for the Proterozoic east Albany-Fraser Orogen, Western Australia, are extracted from ambient seismic noise recorded with the 70-station ALFREX array. This two-year temporary installation provided detailed coverage across the orogen and the edge of the Neoarchean Yilgarn Craton, a region where no passive seismic studies of this scale have occurred to date. The surface wave velocities are rather fast overall ($>$3 km/s nearly everywhere), as expected for exposed Proterozoic basement rocks. No clear signature of the transition between Yilgarn Craton and Albany-Fraser Orogen is observed, but several strong anomalies corresponding to more local geological features were obtained. A prominent, NE-elongated high-velocity anomaly in the northern part of the array is coincident with a Bouguer gravity high caused by the upper crustal metamorphic rocks of the Fraser Zone. This feature disappears towards longer periods, which hints at an exclusively upper crustal origin for this anomaly. Further east, the limestones of the Cenozoic Eucla Basin are clearly imaged as a pronounced low-velocity zone at short periods, but the prevalence of low velocities to periods

of $\geq$5 s implies that the uppermost basement in this area is likewise slow. At longer periods, slightly above-average surface wave velocities are imaged below the Eucla Basin.

Keywords: surface wave tomography, ambient noise, Albany-Fraser Orogen, crustal structure

1 INTRODUCTION

The transition from Archean cratonic blocks to adjacent Proterozoic orogens usually has a clear signature in upper mantle seismic velocities (e.g. Ritsema et al., 1998; Fishwick et al., 2005). Since the upper mantle is relatively homogeneous in terms of composition, seismic velocities are, to first order, determined by the temperature distribution. The mantle lithospheric keels that underlie cratons are colder than their surroundings, and therefore exhibit higher P and S wavespeeds. Elevated shear wavespeeds, usually gleaned from continent-wide studies of surface wave velocities, are thus frequently used to map out the lateral and depth extent of these keels (e.g. Kennett et al., 2013). At crustal depths, the distinction between Archean craton and Proterozoic orogen is significantly less straightforward, and global compilations of seismic wavespeeds show no systematic difference between the two (Rudnick and Fountain, 1995). The main reason for this observation is that the crustal seismic velocity field is primarily controlled by the heterogeneous lithology (e.g. Christensen and Mooney, 1995), and not by temperature. However, there are cases where subtle systematic differences in crustal velocities between craton and adjacent orogen have been identified (e.g. Dalton et al., 2011).

In this study, we use ambient seismic noise recorded with a 70-station seismic array to image the upper and middle crustal surface wave velocity structure of the east Albany-Fraser Orogen, a Proterozoic orogen in southwestern Australia, and its transition to the adjacent Archean Yilgarn Craton. The deployment was designed to complement three active seismic profiles that were shot in 2012 near the northern and southern ends of the array (Figure 1; Spaggiari et al., 2014b). An additional objective of this study is thus to check whether some of the seismic domains identified in the active seismic profiles possess a distinct signature in the surface wave velocities. We further interpret our results together with the regional Bouguer gravity map (Figure 2), which contains several first- and second-order features that are thought to represent intra-crustal density variations that should have an expression in seismic velocities.

2 TECTONIC SETTING

The east Albany-Fraser Orogen (AFO) in Western Australia represents an area of extensive crustal reworking of the Archean Yilgarn Craton's southeastern margin during the Proterozoic (Myers, 1990; Kirkland et al., 2011; Spaggiari et al., 2014a, 2015). Paleoproterozoic tectonism was dominated by extension, whereas Mesoproterozoic tectonism occurred in two stages between 1330-1280 Ma and 1225-1140 Ma (Clark et al., 2000; Kirkland et al., 2011; Spaggiari et al., 2015). Stage I was triggered by arc accretion to the east in the Madura Province, and Stage II was an intracratonic reactivation event (Kirkland et al., 2011; Smithies et al., 2015). The east AFO is subdivided into the Northern Foreland and Kepa Kurl Booya Province, which is further divided into the Tropicana, Biranup, Nornalup and Fraser Zones (Figure 1; Spaggiari et al., 2014a). The Northern Foreland is for the most part Archean Yilgarn Craton that was last modified during the Albany-Fraser Orogeny. In the east Albany-Fraser Orogen it forms a narrow belt between the unmodified Yilgarn Craton and the Kepa Kurl Booya Province. East of the Northern Foreland, the Biranup Zone extends along the entire length of the AFO, comprising mainly orthogneissic rocks with ages of 1810-1625 Ma (Kirkland et al., 2011; Spaggiari et al., 2014a). The eastern Nornalup Zone consists of similar lithologies, but has been more heavily intruded by the granites of the ca. 1330-1280 Ma Recherche and ca. 1200-1140 Ma Esperance Supersuites. In its northeastern part, these rocks are overlain by the Eocene limestone successions of the Eucla Basin. In the south, the Newman and Coramup Shear Zones separate the Biranup and Nornalup Zones, but farther north they are separated by the Fraser Zone, an approximately 450 km long, northeasterly trending belt of high-density, metagabbroic granulite facies rocks (Figure 1) that produce a prominent high in the regional Bouguer gravity map (Figure 2). Bound by the Fraser Shear Zone to the west and south and by the Newman and Boonderoo Shear Zones to the east, this body of mafic to locally ultramafic rocks and coeval metagranitic rocks was exhumed from lower- to mid-crustal depths in the later part of Stage I of the Albany-Fraser Orogeny (Spaggiari et al., 2015; Clark et al., 2014; Maier et al., 2016). To the far east, just beyond the easternmost extent of our seismometer deployment, the Rodona Shear Zone separates the AFO from the adjacent Madura Province.

3 DATA

We used data from the temporary ALFREX deployment (Sippl et al., 2015), a 70-station array that was deployed in the Albany-Fraser Orogen between November 2013 and January 2016. The network consisted of both short-period (1 Hz corner frequency) and broadband sensors (Figure 1) and was run in two periods of approximately one year deployment time each. ALFREX covered all lithotectonic units from the Neoarchean Yilgarn Craton in the west to the eastern Nornalup Zone in the east, and

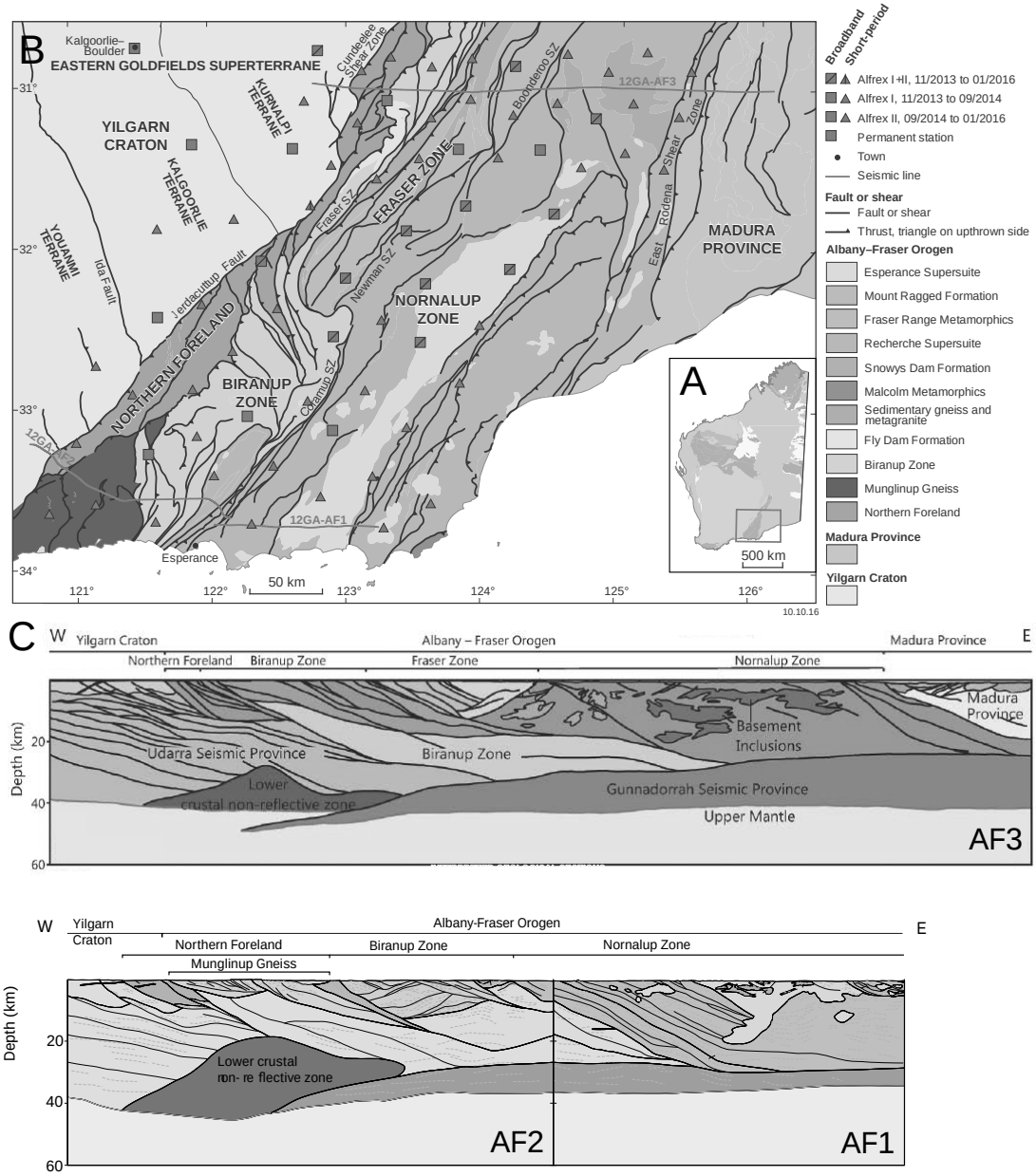

Figure 1. A) Overview tectonic units map of Western Australia, with Archean cratons displayed in light red, Proterozoic orogens in brown and Proterozoic basins in grey and yellow. Younger surface units are shown in blue (modified after Cawood and Korsch, 2008). The red frame outlines the area shown in subfigure B. B) ALFREX station deployment overlain on a simplified regional geology map of the east Albany-Fraser Orogen and its immediate surroundings. Seismic stations are displayed as triangles (short-period stations) and squares (broadband), the colors blue and red refer to the first (11/2013-09/2014) and second (09/2014-01/2016) installation period. Regional permanent stations are shown in green, and the 2012 deep seismic reflection profiles are displayed as red lines. C) Geological interpretation of active seismic lines 12GA-AF1 to -AF3 (positions shown in subfigure A). Figure modified after Spaggiari et al. (2014b).

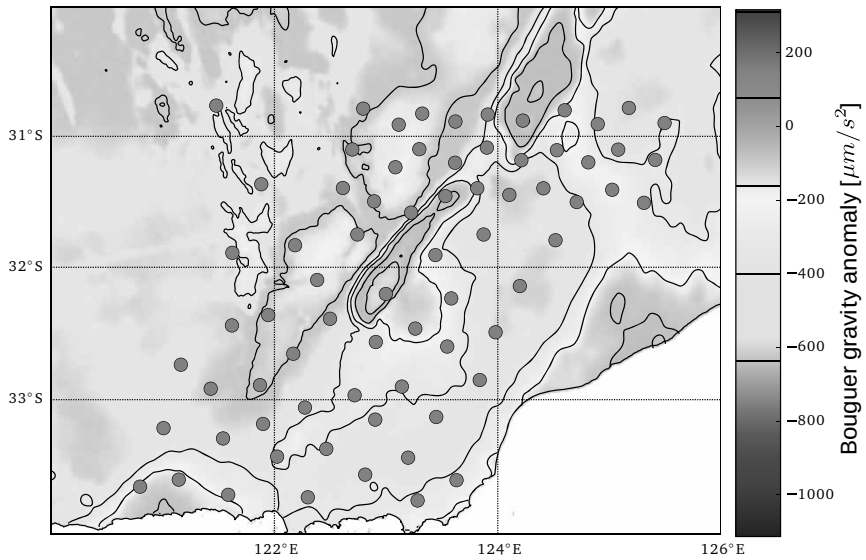

Figure 2. Regional Bouguer gravity anomaly map of the study area, showing the two parallel anomalies of opposite sign mentioned in the text. Locations of seismic stations are shown with red circles. The contour lines displayed here correspond to the contour lines overlain onto the group and phase velocity maps in Figure 8 and Figures S4-S7.

was complemented by two permanent stations (KMBL, AUKAL) at its northwestern edge. 12 stations were operated for the entire period of 2 years, providing raypath connectivity between the two sub-networks (Figure S3).

4 METHOD

We retrieved empirical Green's functions for fundamental mode Rayleigh waves from cross-correlations of vertical-component traces of ambient seismic noise using all possible station pair combinations in our dataset. Hourly data segments were demeaned and detrended, the instrument response was removed, traces were downsampled from 50 to 10 Hz and bandpass fi ltered to between 0.01 and 1 Hz before correlation. Amplitudes were normalized by multiplying with the inverse of a moving-window amplitude average (Bensen et al., 2007), and spectral whitening was applied. The cross correlation was performed with a time domain routine within the ObsPy software package (Beyreuther et al., 2010), hourly correlograms were stacked for the entire available time period. Examples of retrieved empirical Green's functions (EGFs) are shown in Figure 3. Since we have many short-period instruments in the dataset, we restricted the used period range to 2-20 seconds. Correlograms for short-period stations at the longest periods have lower signal-to-noise ratios compared to the broadband stations, but are frequently still utilizable. Group velocities were determined using frequency-time analysis (FTAN,

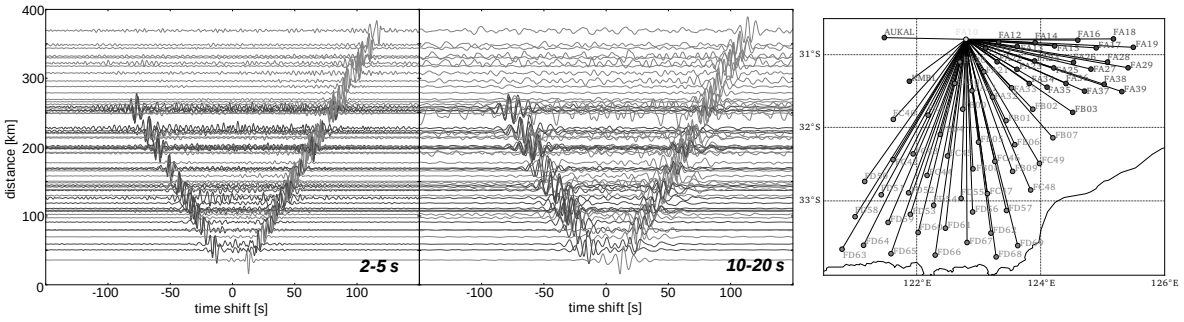

Figure 3. Example of noise cross-correlations between station FA10 and all other stations (see map in bottom subfigure) for two different period bands (2-5s and 10-20s). Although the majority of utilized stations had short-period sensors, reasonably good signal-to-noise ratio could be achieved down to periods of 20 seconds. Nearly all acquired cross-correlation traces are asymmetric, with stations from southern directions showing the stronger signal in the causal branch (red traces and red labels in the map), corresponding to a predominance of noise sources in the south. Station pairs with ray paths oriented more in east-west direction (blue traces and labels) show stronger signal in the anti-causal branch of the cross-correlations, which corresponds to noise sources located to the west. In both cases, the proximity to the ocean can explain the observed trend, since the study area is situated in the southwestern corner of the Australian continent (see Figure 1A).

e.g. Levshin et al., 1992) and a phase-matched filtering approach (Levshin and Ritzwoller, 2001; Arroucau et al., 2010; Young et al., 2011) on the envelope of the symmetric component (averaged causal and acausal parts) of the empirical Green's functions. Only cross-correlograms between stations with a spatial separation larger than 3 wavelengths were used for the retrieval of dispersion curves (e.g. Lin et al., 2008; Bensen et al., 2008), and traces with a signal-to-noise ratio (SNR) lower than 4 were discarded. This rather low choice of SNR was necessary to have sufficient paths available at the longer periods. Group velocities were determined twice, once without and once with the phase-matched filtering, and only measurements that were consistent between the two approaches were kept. All selected group velocity dispersion curves are shown in Figure S1 in the Supplementary Material.

For determining phase velocities, we relied on a semi-automated approach (modified from Arroucau et al., 2010; Young et al., 2011) that picks phase velocity dispersion curves from plots of phase velocity against period (after Yao et al., 2006). We first carefully handpicked an average dispersion curve, based on which a corridor of "sensible" velocities was established. Dispersion curves from all station pairs were then picked automatically, whereby the resulting velocity was required to lie in the aforementioned corridor. All thus determined curves were visually checked and modified if necessary. If several branches were clearly visible in the matrix plot of phase velocity against period, we picked the slowest one that featured increasing phase velocities with period. A plot of all selected phase velocity dispersion curves is provided in Figure S1.

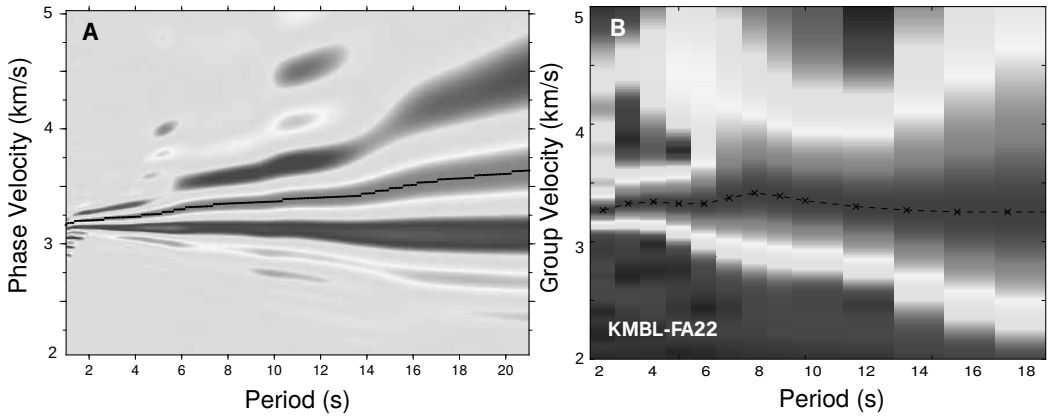

Figure 4. Examples for phase (A) and group velocity (B) determination. EGFs or their envelopes (in B) are plotted against period, and maximum positive amplitudes (red in both plots) are picked.

Examples for single group and phase velocity dispersion curve picks are shown in Figure 4. The distribution of phase and group velocities across our network is summarized as a median dispersion curve in Figure 5. The wavelength criterion applied to the phase and group velocity determination means that the largest numbers of picks were obtained for the shorter periods between 4-7 s (Figure 6), and path coverage significantly decreases for the longer periods (Figure S3). The median dispersion curves hint at overall high to very high surface wave velocities. We inverted for two-dimensional distributions of group and phase velocity at periods between 2 and 20 seconds, using the iterative non-linear code `fmst` which employs a fast-marching method for the forward calculations (Rawlinson and Kennett, 2004; Rawlinson and Sambridge, 2005) and a subspace method (e.g. Kennett et al., 1988) for the actual inversion of surface wave velocities. The study area was parameterized as a regular grid of 60*60 nodes, which corresponds to grid cell sizes close to 10 km in both latitudinal and longitudinal direction. The tomographic inversion was performed with a total of 10 iterations, using a homogeneous starting model set to the mean velocity of all travel times at each period. After each iteration, theoretical traveltimes were recomputed. Optimal values for smoothing and damping were chosen by analyzing L-curves between data and model variance (after Eberhart-Phillips, 1986). Achieved variance reductions compared to the homogeneous starting model ranged between 89 and 38% for phase velocities and between 85 and 20% for group velocities, with the latter featuring substantially lower numbers at the longest periods (see Figure 6). This is due both to a lower number of raypaths and a higher uncertainty in the group velocity picks at long periods (especially at 12 and 14s; see Figures 5 and S1) compared to the phase velocity ones (Figure 4). A summary plot of the residual distributions before and after inversion is provided in Figure 7.

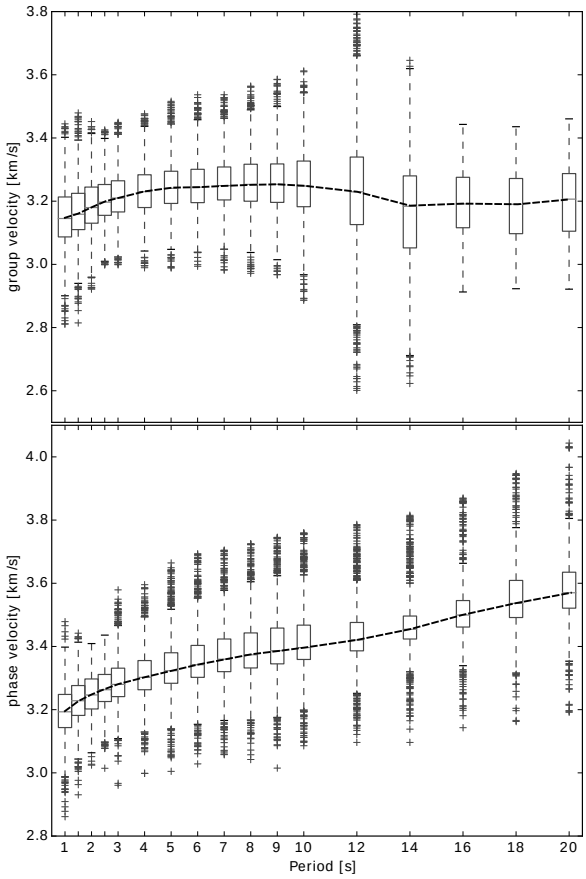

Figure 5. Median dispersion curves for group velocities (upper panel) and phase velocities (lower panel) for the entire ALFREX array. For every period, a boxplot of the distribution of retrieved velocities is shown. The black dashed line connects the median values (red horizontal lines in the boxplots) for the different periods.

5 RESOLUTION TESTS

Results for checkerboard resolution tests for the retrieval of phase and group velocity maps at 2, 5, 10 and 20 seconds period are shown in Figure S2 (Supplementary Material). We used the same event-station geometry, inversion settings and damping/smoothing combination as for the real data, with input anomalies of $\pm 7.5\%$ superimposed onto the mean velocity at each period. Input anomalies measured 2*2 nodes (corresponding to about 20*20 km), with one neutral node between anomalies of opposite sign. Gaussian noise with a standard deviation of 0.5 s (for 2 and 5 s period), 0.7 s (for 10 s period) or 1.0 s (for 20 s period) was added to the synthetic travel times to simulate the uncertainty in retrieving the correct phase and group velocities. The retrieved images show a noticeable reduction in resolution at the period of 20 s, where diagonal smearing of anomalies and the coalescence of single vertices can be observed. This is mostly due to the substantially lower number of rays that were inverted at this period. At shorter periods, the input anomalies are reasonably well recovered over most

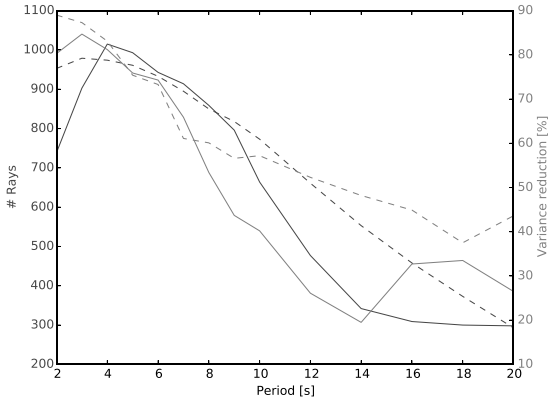

Figure 6. Plot of achieved variance reduction (red) and the number of station pairs used (blue) for group velocity (solid lines) and phase velocity (dashed lines) inversion at different periods. The number of usable station combinations decreases with period due to the wavelength criterion, which, together with higher uncertainties in the traveltime picks (see Figure 4) leads to lower variance reductions. Phase velocity inversions perform better than group velocity inversions at longer periods.

of the study area, although with somewhat reduced amplitudes. The results from the group velocity inversion appear to be better resolved than the phase velocity images. The main reason for this is that the L-curve analysis yielded higher optimal damping values for the phase velocities at shorter periods, which was likely to be due to more scatter in the picks (see Figure S1). At the northwestern edge of the network, the available resolution is consistently low, due to ray path coverage to and from a single station only (see Figure S3). Therefore anomalies retrieved in this region have been omitted from the interpretations.

6 GROUP AND PHASE VELOCITY MAPS

Group and phase velocity maps for periods of 2, 5, 10 and 20 s are shown in Figure 8, maps for other periods can be found in the Supplementary Material (Figures S4-S7). All phase and group velocity maps feature quite high average velocities clearly in excess of 3 km/s even for the shortest period of 2 s. These results confi rm the anomalously high group velocities at short periods for most of Western Australia found by Saygin and Kennett (2012). Whereas phase velocities increase with period, the average group velocity dispersion curve is nearly fl at (Figure 5). The main features in the group and phase velocity maps are highly consistent, although there are differences in detail; this attests to the robustness of the retrieved velocity distributions.

The most prominent anomaly is a pronounced elongated velocity high, trending NNE in the northern half of the array (anomaly H1 in Figure 8), which is spatially coincident with a regional gravity high

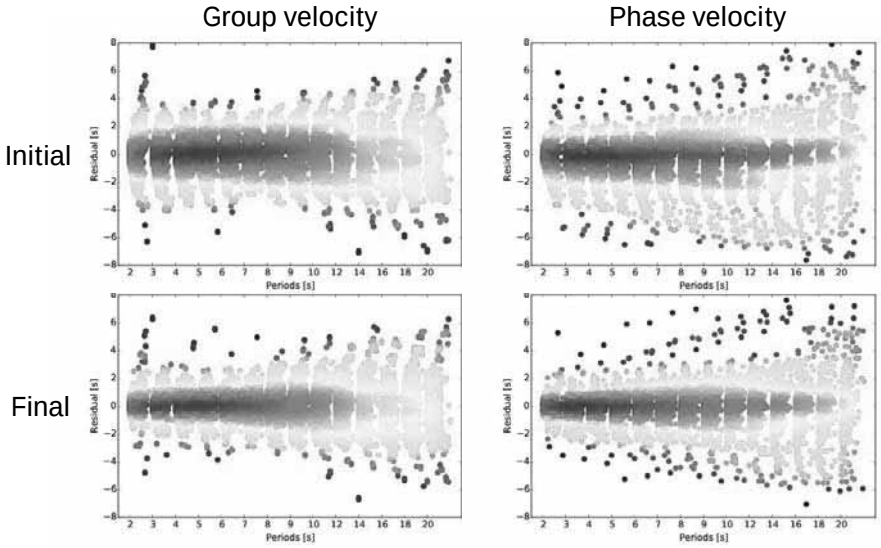

Figure 7. Initial (upper row) and final (lower row) residual distributions for group (left column) and phase velocity (right column) inversions. For every period, travel time residuals are plotted against travel times, color coding of points is according to point density. It is apparent that while the residual distribution is significantly narrowed down for short periods, the effect is smaller for the longer periods.

(shown with orange contour lines in Figure 8). While this anomaly can be traced from the southern end of the gravity high up to the northern end of the array in the 2 and 5 s maps, its northern part fades out in the 10 s phase velocity map, but is still clearly observed in the group velocities. At 20 s period, the anomaly is no longer visible. In most of the group and phase velocity maps, this high-velocity anomaly protrudes westward into the adjacent gravity low (H2). In the eastern and northeastern part of the array, where the Nornalup Zone is overlain by the limestones of the Eucla Basin, consistently low velocities are retrieved at short (L1) and the longest periods (L3), whereas velocities between those (i.e. at 10 s) are fast to intermediate. In the southern and western part of the study area, retrieved velocities usually do not deviate far from the mean for each period. In the far southeast of the array, an area of consistently low velocities in the vicinity of Cape Arid (L2) is imaged at all periods. The prominent high-velocity anomaly in the northwest in the 20 s phase velocity map (H3) lies in a region of low resolution (Figure S2) and poor ray coverage (Figure S3) and is therefore not robust.

7 DEPTH INVERSIONS

In order to better understand at which depths the imaged anomalies originate, we calculated sensitivity kernels for phase and group velocities (Figure 9) and carried out depth inversions of dispersion curves for 6 characteristic locations (Figure 10). Figure 9 shows sensitivity kernels for phase and group velocities at the periods displayed in Figure 8, computed using the codes of Herrmann (2013) and a

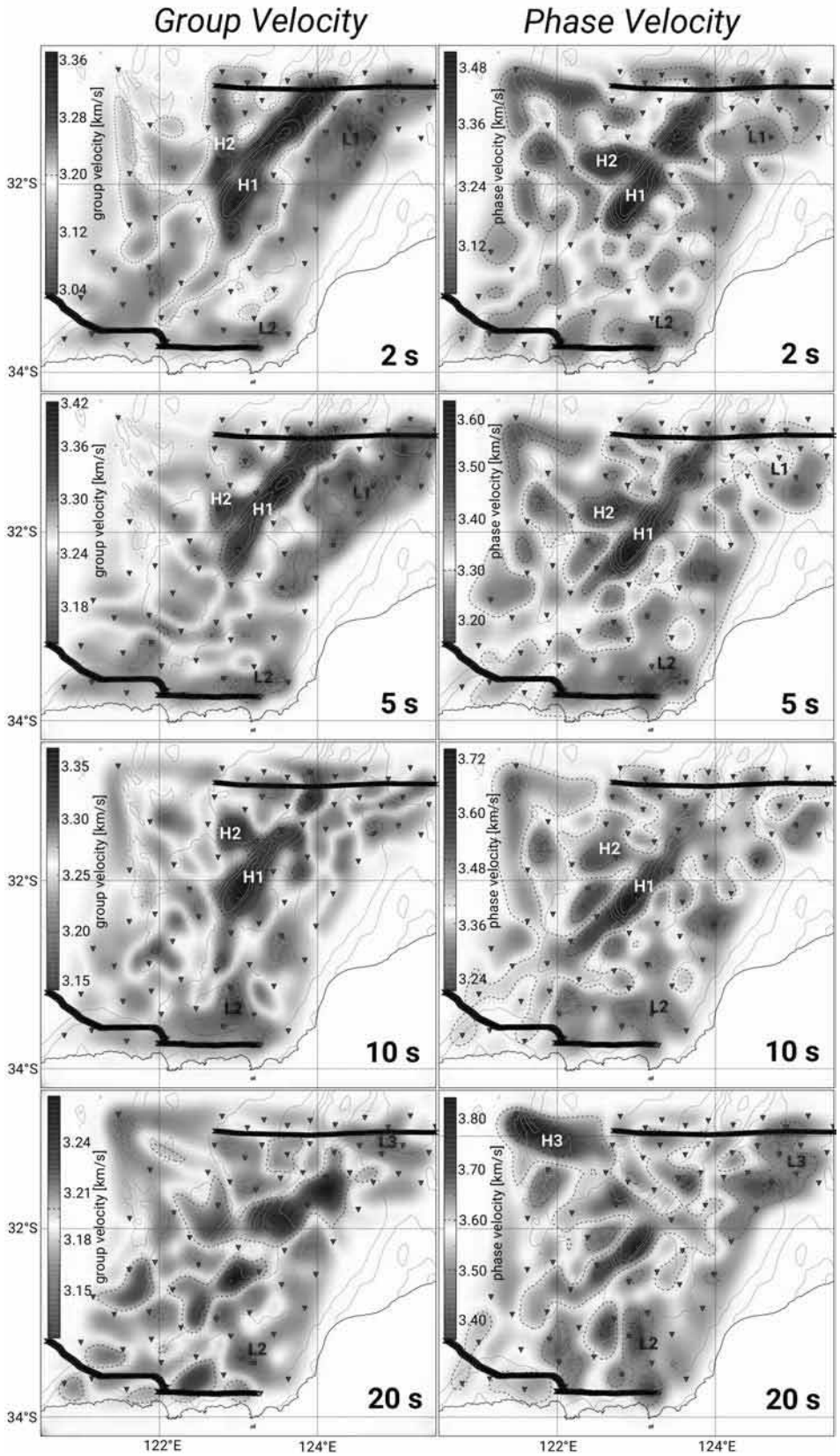

Figure 8. Group velocity maps (left column) and phase velocity maps (right column) for periods of 2, 5, 10 and 20 s. The Bouguer gravity contours are overlain in orange (positive anomalies) and green (negative anomalies). The velocity color scales are normalized so that the mean velocity in each image appears in white, and black dashed isolines are shown every 0.1 km/s. The inverted green triangles represent the seismic stations we used, thick black lines mark the location of the 2012 deep seismic reflection profiles. Raypath coverage for each of these maps is shown in Figure S3. High- and low-velocity anomalies discussed in the text are numbered.

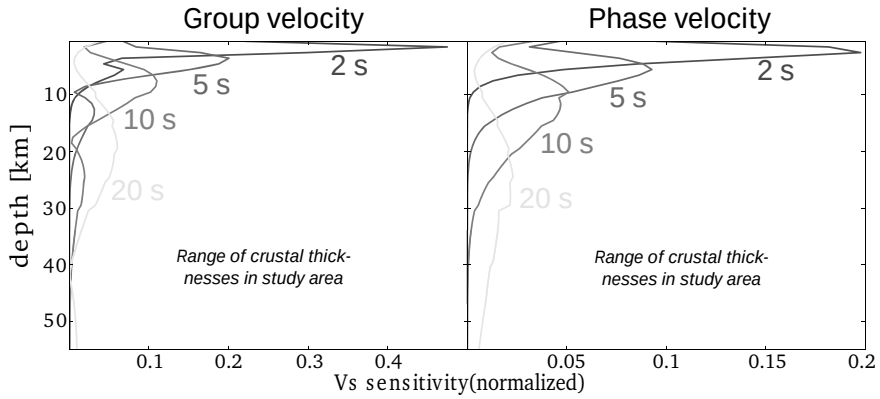

Figure 9. Sensitivity kernels for group (left) and phase velocities (right), computed using the code from Herrmann (2013) and assuming a 1D velocity model that represents the regional average over the study area, taken from the continent-wide AusREM model (Salmon et al., 2013). Range of Moho depths in the study area is taken from Sippl et al. (2017).

regional average over the AusREM velocity model (Salmon et al., 2013) as background. Tests showed that the kernels only weakly depend on the utilized background velocity model, a computation using a global model yielded highly similar results. These sensitivity kernels show that the period range that we analyzed is mainly sampling the upper and middle crust, with only a weak contribution from lower crustal depths at the longest periods. The infl uence of subcrustal regions and thus Moho topography is nearly non-existent for group velocities, and small for the phase velocities. As expected, group velocities generally sample somewhat shallower depths than phase velocities for the same period.

We inverted group velocity dispersion curves picked at 6 characteristic grid nodepoints throughout the study area for 1D v_s profi les (similar to, e.g., Domingues et al., 2016, see Figure 10). The applied 1D inversion scheme is a linearized, damped least-squares approach (Herrmann, 2013), with which we performed a total of 12 iterations. After these, the changes in the resulting v_s models were minimal. The starting model was homogeneous, with v_s=3.53 km/s in 8 layers of 3 km thickness each. At depths larger than 24 km, v_s was kept fi xed at the same value. We applied this strategy because of the limited resolution of our dataset at lower crustal and sub-crustal depths, due to the limited range of utilized periods (see Figure 9). The retrieved v_s profi les show pronounced differences between the various regions: both points taken within the Fraser Zone (green), for instance, feature high shear wavespeeds in the uppermost 12-15 km, underlain by significantly slower material. The 1D profile located in the Eucla Basin, on the other hand, exhibits a very slow uppermost layer, but rather high velocities in the deeper part of the upper crust (magenta curve). Nearly all profiles show a decrease in shear wave velocities towards middle crustal depths.

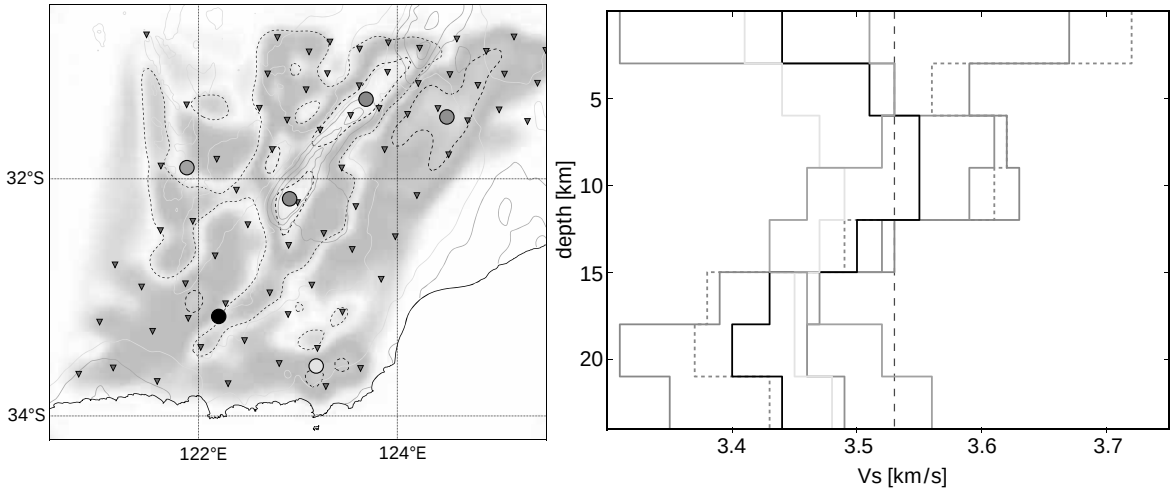

Figure 10. (Left) Location of the six group velocity dispersion curves (shown with colored dots) that were inverted for 1D shear velocity profi les, plotted on top of the group velocity map at 2 s period. (Right) Retrieved 1D shear wave velocity profi les. The color of the profi le curves corresponds to the color of the dots in the left subfi gure; the dashed green curve corresponds to the northern one of the two dots in the Fraser Zone high velocity anomaly, the solid line to the southern one. The vertical dashed blue line marks the velocity of the homogeneous starting model.

8 DISCUSSION

We find no clear signature of the transition between Archean Yilgarn Craton and Proterozoic Albany-Fraser Orogen in our phase and group velocity maps. The maps are instead dominated by anomalies that represent more regional geological features that will be discussed in the following. Previous knowledge of the regional crustal structure comes predominantly from three active seismic lines (12GA-AF1, 12GA-AF2 and 12GA-AF3) acquired in 2012 (Figure; 1 Spaggiari et al., 2014b), as well as from surface geological constraints. We thus fi rst interpret the obtained results based on these two datasets, and attempt to use the phase and group velocity maps to derive the distribution of units between the seismic profi les. In a second step, we compare the obtained anomalies to the regional Bouguer gravity map, which allows the placement of depth constraints on some of the gravity anomalies.

8.1 Interpretation of retrieved anomalies

Anomaly H1, the most prominent high-velocity anomaly we image, is clearly associated with the Fraser Zone (see Figure 1), which is in part defi ned by its distinct regional high in Bouguer gravity maps (Figure 2). The metagabbroic rocks that dominate the Fraser Zone have very high rock densities,

thus creating a positive surface wave anomaly, even in the presence of locally elevated v_p/v_s ratio (Sippl et al., 2017). In active seismic line 12GA-AF3, which crosses the Fraser Zone in the northernmost part of our array, the Fraser Zone is imaged as a V-shaped entity (Figure 1C) interpreted as a pop-up structure with a maximum depth of 4.2 s two-way travel time (TWT), approximating 13 km depth (based on a conversion velocity of 6 km/s; Spaggiari et al., 2014b). In the phase and group velocity maps, the high-velocity anomaly associated with the Fraser Zone extends to longer periods in its southern part compared to the location where the active seismic profile crosses (central part of the Fraser Zone; Figure 8). This is in accordance with the higher amplitudes of the gravity high in the southernmost part of the Fraser Zone, and may provide insight into the geometrical configuration of the Fraser Zone rocks and their exhumation. Alternatively, the Fraser Zone may simply be thicker in this region, regardless of the exhumation mechanism, as there are no significant differences in the observed geological relationships between its central and southern portions, i.e. there is nothing to suggest a different crustal level is exposed (Maier et al., 2016). However, the two 1D v_s profiles located in the northeastern and southwestern part of the Fraser Zone (Figure 10) both show anomalously fast velocities confined to the uppermost 12-15 km, underlain by significantly slower material. No clear difference in depth extent of the elevated velocities is discernible.

The most prominent low-velocity anomaly we image (L1) is situated at shallow crustal levels throughout the eastern Nornalup Zone, approximately where the eastern Nornalup Zone is overlain by the Eocene sedimentary rocks of the Eucla Basin. Drillcores from boreholes to the east, where the basin is expected to be deeper, showed that the basement is reached at depths around 400-500 m there (Spaggiari and Smithies, 2015), and a recent study by Scheib et al. (2016) retrieved depths to basement of $\leq$300 m for the part of the Eucla Basin that is situated in our study area. Thus, the fact that we still see consistently slow velocities at 5 s period most likely implies a slow uppermost basement in addition to the overlying sediments. The 1D v_s profile for the Eucla Basin (Figure 10; magenta curve) shows a very slow uppermost layer, and faster velocities from 6 km downwards. Information on the nature of the basement beneath the Eucla Basin is very sparse, including that beneath the northeastern Nornalup Zone. Potential field and sparse drillcore data suggest considerable complexity, including the presence of metasedimentary rocks intruded by dominantly granitic rocks of the Recherche and Esperance Supersuites (Spaggiari et al., 2014b; Murdie et al., 2014; Spaggiari and Smithies, 2015). The transition from intermediate to fast velocities at 10 s, which most likely represent the basement, to markedly slow velocities at 20 s (L3) likely captures a vertical transition in the middle crust that has not been previously recognized. Such a transition may, at least in part, explain significant areas of reflectivity that are mostly restricted to the upper crust in the area near L1 in the active seismic line

12GA-AF3. These areas of reflectivity were interpreted as metasedimentary rocks in the uppermost crust, underlain by inclusions of basement within younger granites (Spaggiari et al., 2014b). The low-velocity anomaly beneath the Cape Arid region (L2) in the very southeast of the array is enigmatic. While the region shows a local minimum of crustal thickness (Sippl et al., 2017), the active seismic profile 12GA-AF1 only extends as far as the western edge of this anomaly (Spaggiari et al., 2014b; Waddell et al., 2015). However, the far eastern end of the 12GA-AF1 profile shows a change in upper and lower crustal character that might correspond to the anomalously slow velocities we image here. In the 1D v_s profile, this region exhibits velocities slower than adjacent areas throughout the upper crust, to a depth of 15 km.

8.2 Comparison with Bouguer gravity

Directly relating a distribution of seismic velocities to density is not a straightforward task. Although empirically determined regression curves exist that yield density values depending on v_p and/or v_s (Nafe and Drake, 1957; Brocher, 2005), density also varies between different rock types at the same seismic velocity, which leads to scatter around those regression curves that is often significantly larger than the anomalies one seeks to explain (e.g. Barton, 1986). In the east Albany-Fraser Orogen, the largest and most characteristic gravity anomalies are a pair of parallel, elongated anomalies of opposite sign that follow the general strike of the orogen (Figure 2). These have been explained as due to a regionally thickened crust (responsible for the gravity low) in combination with dense upper crustal rocks in the Fraser Zone (Sippl et al., 2017). While we do not resolve the crustal structure down to Moho depths here (Figure 9), we clearly image the elevated seismic velocities of the Fraser Zone in the upper crust (anomaly H1; see above).

The two dense units in the lower crust retrieved in the gravity models in Sippl et al. (2017), the Gunnadorrah seismic zone that underlies the east AFO and the denser lower crustal rocks inside the Moho "trough" imaged with receiver functions, show no signature in our velocity models. This is not surprising because they are situated at depths below of what we can expect to resolve. However, the Bouguer gravity map helps identify the origin of anomaly H2 (Figure 8). This high-velocity anomaly extends west of the Fraser Zone gravity high, and is situated slightly south of an area where a localized, northwesterly trending gravity high intersects the otherwise continuous gravity low that parallels the western side of the Fraser Zone (see Figure 2). This local gravity high corresponds to the location where northwesterly trending greenstone belts of the Eastern Goldfields Superterrane extend as far southeast as the Cundeelee Shear Zone (Figure 1), with the reworked counterparts most likely dipping to the southeast beneath the shear zone (see also Spaggiari et al., 2014b). It is also interesting to note

that some features in the Bouguer gravity map do not appear to have a signature in our velocity maps, which could imply that they have a deeper, lower crustal origin. This applies to the prominent gravity low along the orogen's strike (see above), the gravity high in the far southwest of the array which has been linked to high-density lower crustal rocks (Sippl et al., 2017), and to the extension of the Fraser Zone gravity high to the southeast, which has previously been modelled as originating from a mid- to lower-crustal high-density body (Brisbout, 2015).

9 CONCLUSIONS

We inverted group and phase velocity wavespeeds obtained from ambient noise cross-correlation of station pairs of the ALFREX passive seismic deployment (2013-2016) in the east Albany-Fraser Orogen to obtain 2D maps of phase and group velocities at periods between 2 and 20 s. Furthermore, we tried to constrain the depth extent of the retrieved anomalies by the calculation of sensitivity kernels and by carrying out inversions for 1D v_s profiles at characteristic positions.

The major surface wave velocity variations across the Albany-Fraser Orogen do not show a sharp transition between Neoarchean and Proterozoic rocks, as one might expect from their juxtaposition shown in geological maps. Instead, surface-wave velocities mainly delineate several local features and lithological units. This could be due to the fact that the AFO crust actually contains large volumes of Neoarchean material, particularly in the lower crust, that has been thermally and structurally reworked. The most prominent surface wavespeed anomalies we retrieved correspond to the Fraser Zone metamorphic rocks and the limestone and sediment successions of the Eucla Basin atop the eastern Nornalup Zone. The Fraser Zone is outlined by clearly elevated seismic velocities in the upper crust, to depths of 12-15 km. The extent of elevated surface wave velocities corresponds to the area outlined by a gravity high, which is evidence for a link between rock type and velocity here. Other prominent anomalies in the eastern part of the array are indicative of the sediment cover and basement structure of the easter Nornalup Zone. While it is not always possible to link the units from the active seismic profiles (Figure 1C) to a distinct velocity signature, the phase and group velocity maps from ambient noise tomography have proven useful in placing depth constraints on anomalies observed in the Bouguer gravity maps, and outlining a number of regional features more clearly.

ACKNOWLEDGMENTS

This study was funded through ARC Linkage Grant LP130100413 and the Geological Survey of Western Australia. The Bouguer gravity anomaly map plotted in Figure 2 is provided by Geoscience

Australia (http://www.ga.gov.au/data-pubs/data-compilations/geophysics). We thank the various field crews who helped with data collection and the ANSIR instrument pool for the recorders and seismometers. C.V. Spaggiari and K. Gessner publish with the permission of the Director of the Geological Survey of Western Australia. Comments from two anonymous reviewers and the associate editor, Ana Ferreira, helped to considerably improve the manuscript.

References

Arroucau, P., Rawlinson, N., Sambridge, M., 2010. New insight into Cainozoic sedimentary basins and Palaeozoic suture zones in southeast Australia from ambient noise surface wave tomography. Geophysical Research Letters 37, 1–6.

Barton, P.J., 1986. The relationship between seismic velocity and density in the continental crust - a useful constraint? Geophysical Journal of the Royal Astronomical Society 87, 195–208.

Bensen, G.D., Ritzwoller, M.H., Barmin, M.P., Levshin, A.L., Lin, F.C., Moschetti, M.P., Shapiro, N.M., Yang, Y., 2007. Processing seismic ambient noise data to obtain reliable broad-band surface wave dispersion measurements. Geophysical Journal International 169, 1239–1260.

Bensen, G.D., Ritzwoller, M.H., Shapiro, N.M., 2008. Broadband ambient noise surface wave tomography across the United States. Journal of Geophysical Research 113, B05306.

Beyreuther, M., Barsch, R., Krischer, L., Megies, T., Behr, Y., Wassermann, J., 2010. ObsPy: A Python Toolbox for Seismology. Seismological Research Letters 81, 530–533.

Brisbout, L., 2015. Determining crustal architecture in the east albanyfraser orogen from geological and geophysical data.

Brocher, T.M., 2005. Empirical relations between elastic wavespeeds and density in the Earth's crust. Bulletin of the Seismological Society of America 95, 2081–2092.

Cawood, P.A., Korsch, R.J., 2008. Assembling Australia: Proterozoic building of a continent. Precambrian Research 166, 1–35.

Christensen, N.I., Mooney, W.D., 1995. Seismic velocity structure and composition of the continental crust; a global view. Journal of Geophysical Research 100, 9761–9788.

Clark, C., Kirkland, C.L., Spaggiari, C.V., Oorschot, C., Wingate, M., Taylor, R.J., 2014. Proterozoic granulite formation driven by mafic magmatism: An example from the Fraser Range Metamorphics, Western Australia. Precambrian Research 240, 1–21.

Clark, D.J., Hensen, B.J., Kinny, P.D., 2000. Geochronological constraints for a two-stage history of the Albany-Fraser Orogen, Western Australia. Precambrian Research 102, 155–183.

Dalton, C.A., Gaherty, J.B., Courtier, A.M., 2011. Crustal Vs structure in northwestern Canada:

Imaging the Cordillera-craton transition with ambient noise tomography. Journal of Geophysical Research: Solid Earth 116, 1–30.

Domingues, A., Silveira, G., Ferreira, A.M.G., Chang, S.J., Custodio, S., Fonseca, J.F.B.D., 2016. Ambient noise tomography of the East African Rift in Mozambique. Geophysical Journal International 204, 1565–1578.

Eberhart-Phillips, D., 1986. Three-Dimensional Velocity Structure in Northern California Coast Ranges From Inversion of Local Earthquake Arrival Times. Bulletin of the Seismological Society of America 76, 1025–1052.

Fishwick, S., Kennett, B.L.N., Reading, A.M., 2005. Contrasts in lithospheric structure within the Australian craton - Insights from surface wave tomography. Earth and Planetary Science Letters 231, 163–176.

Herrmann, R.B., 2013. Computer Programs in Seismology: An Evolving Tool for Instruction and Research. Seismological Research Letters 84, 1081–1088.

Kennett, B.L.N., Fichtner, A., Fishwick, S., Yoshizawa, K., 2013. Australian seismological referencemodel (AuSREM): Mantle component. Geophysical Journal International 192, 871–887.

Kennett, B.L.N., Sambridge, M., Williamson, P.R., 1988. Subspace Methods for large inverse problems with multiple parameter classes. Geophysical Journal International 94, 237–247.

Kirkland, C.L., Spaggiari, C.V., Pawley, M., Wingate, M., Smithies, R.H., Howard, H., Tyler, I.M., Belousova, E.A., Poujol, M., 2011. On the edge: U-Pb, Lu-Hf, and Sm-Nd data suggests reworking of the Yilgarn craton margin during formation of the Albany-Fraser Orogen. Precambrian Research 187, 223–247.

Levshin, A.L., Ratnikova, L., Berger, J., 1992. Peculiarities of surface-wave propagation across central Eurasia. Bulletin of the Seismological Society of America 82, 2464–2493.

Levshin, A.L., Ritzwoller, M.H., 2001. Automated Detection, Extraction, and Measurement of Regional Surface Waves BT - Monitoring the Comprehensive Nuclear-Test-Ban Treaty: Surface Waves. Monitoring the Comprehensive Nuclear-Test-Ban Treaty: Surface Waves 158, 1531–1545.

Lin, F.C., Moschetti, M.P., Ritzwoller, M.H., 2008. Surface wave tomography of the western United States from ambient seismic noise: Rayleigh and Love wave phase velocity maps. Geophysical Journal International 173, 281–298.

Maier, W.D., Smithies, R.H., Spaggiari, C.V., Barnes, S.J., Kirkland, C.L., Yang, S., Lahaye, Y., Kiddie, O., MacRae, C., 2016. Petrogenesis and Ni-Cu sulphide potential of mafic-ultramafic rocks in the Mesoproterozoic Fraser Zone within the Albany-Fraser Orogen, Western Australia. Precambrian Research 281, 27–46.

Murdie, R., Gessner, K., Occhipinti, S., Spaggiari, C.V., Brett, J., 2014. Interpretation of gravity

and magnetic data across the Albany-Fraser Orogen, in: Spaggiari, C.V., Tyler, I.M. (Eds.), Albany-Fraser Orogen Seismic and Magnetotelluric (MT) workshop 2014: extended abstracts. Geological Survey of Western Australia, Perth, Record 2014/06, pp. 118–134.

Myers, J.S., 1990. Precambrian tectonic evolution of part of Gondwana, southwestern Australia. Geology 18, 537–540.

Nafe, J.E., Drake, C.L., 1957. Variation with depth in shallow and deep water marine sediments of porosity, density and the velocities of compressional and shear waves. Geophysics 22, 523–552.

Rawlinson, N., Kennett, B.L.N., 2004. Rapid estimation of relative and absolute delay times across a network by adaptive stacking. Geophysical Journal International 157, 332–340.

Rawlinson, N., Sambridge, M., 2005. The fast marching method: an effective tool for tomographic imaging and tracking multiple phases in complex layered media. Exploration Geophysics 36, 341.

Ritsema, J., Nyblade, A.a., Owens, T.J., Langston, C., VanDecar, J.C., 1998. Upper mantle seismic velocity structure beneath Tanzania, east Africa: Implications for the stability of cratonic lithosphere. Journal of Geophysical Research 103, 21,201–21,213.

Rudnick, R.L., Fountain, D.M., 1995. Nature and composition of the continental crust: A lower crustal perspective. Reviews of Geophysics 33, 267.

Salmon, M., Kennett, B.L.N., Saygin, E., 2013. Australian Seismological Reference Model (AuSREM): crustal component. Geophysical Journal International 192, 190–206.

Saygin, E., Kennett, B.L.N., 2012. Crustal structure of Australia from ambient seismic noise tomography. Journal of Geophysical Research 117, 1–15.

Scheib, A., Morris, P., Murdie, R., Delle Piane, C., 2016. A passive seismic approach to estimating the thickness of sedimentary cover on the Nullarbor Plain, Western Australia. Australian Journal of Earth Sciences 63, 583–598.

Sippl, C., Brisbout, L., Spaggiari, C., Gessner, K., Tkalčić, H., Kennett, B.L.N., Murdie, R., 2017. Crustal structure of a Proterozoic craton boundary: East Albany-Fraser Orogen, Western Australia, imaged with passive seismic and gravity anomaly data. Precambrian Research 296, 78–92.

Sippl, C., Kennett, B.L.N., Tkalčič, H., Spaggiari, C.V., Gessner, K., 2015. New constraints on the current stress field and seismic velocity structure of the eastern Yilgarn Craton from mechanisms of local earthquakes. Australian Journal of Earth Sciences 62, 921–931.

Smithies, R.H., Spaggiari, C.V., Kirkland, C.L., 2015. Building the crust of the AlbanyFraser Orogen; constraints from granite geochemistry. Technical Report. Geological Survey of Western Australia Report 150. Perth.

Spaggiari, C.V., Kirkland, C.L., Smithies, R.H., Occhipinti, S., Wingate, M., 2014a. Geological framework of the Albany-Fraser Orogen, in: Spaggiari, C.V., Tyler, I.M. (Eds.), Albany-Fraser Oro-

gen Seismic and Magnetotelluric (MT) workshop 2014: extended abstracts. Geological Survey of Western Australia, Perth, Record 2014/06, pp. 12–27.

Spaggiari, C.V., Kirkland, C.L., Smithies, R.H., Wingate, M., Belousova, E.A., 2015. Transformation of an Archean craton margin during Proterozoic basin formation and magmatism: The AlbanyFraser Orogen, Western Australia. Precambrian Research 266, 440–466.

Spaggiari, C.V., Occhipinti, S., Korsch, R.J., Doublier, M.P., Clark, D.J., Dentith, M.C., Gessner, K., Doyle, M., Tyler, I.M., Kennett, B.L.N., Costelloe, R.D., Fomin, T., Holzschuh, J., 2014b. Interpretation of Albany-Fraser seismic lines 12GA-AF1, 12GA-AF2 and 12 GA-AF3: implications for crustal architecture, in: Spaggiari, C.V., Tyler, I.M. (Eds.), Albany-Fraser Orogen Seismic and Magnetotelluric (MT) workshop 2014: extended abstracts. Geological Survey of Western Australia, Perth, Record 2014/06, pp. 28–51.

Spaggiari, C.V., Smithies, R.H., 2015. Eucla Basement Stratigraphic Drilling Results Release Workshop: Extended Abstracts. Geological Survey of Western Australia, Perth, Record 2015/10.

Waddell, P.J.A., Timms, N.E., Spaggiari, C.V., Kirkland, C.L., Wingate, M., 2015. Analysis of the Ragged Basin, Western Australia: Insights into syn-orogenic basin evolution within the Albany-Fraser Orogen. Precambrian Research 261, 166–187.

Yao, H., Beghein, C., van der Hilst, R., 2006. Surface wave array tomography in SE Tibet from ambient seismic noise and two-station analysis - II. Crustal and upper-mantle structure. Geophysical Journal International 173, 205–219.

Young, M.K., Rawlinson, N., Arroucau, P., Reading, A.M., Tkalčič, H., 2011. High-frequency ambient noise tomography of southeast Australia: New constraints on Tasmania's tectonic past. Geophysical Research Letters 38, 1–6.